

## Elastic wave-mode separation for VTI media

Jia Yan<sup>1</sup> and Paul Sava<sup>1</sup>

### ABSTRACT

Elastic wave propagation in anisotropic media is well represented by elastic wave equations. Modeling based on elastic wave equations characterizes both kinematics and dynamics correctly. However, because P- and S-modes are both propagated using elastic wave equations, there is a need to separate P- and S-modes to efficiently apply single-mode processing tools. In isotropic media, wave modes are usually separated using Helmholtz decomposition. However, Helmholtz decomposition using conventional divergence and curl operators in anisotropic media does not give satisfactory results and leaves the different wave modes only partially separated. The separation of anisotropic wavefields requires more sophisticated operators that depend on local material parameters. Anisotropic wavefield-separation operators are constructed using the polarization vectors evaluated at each point of the medium by solving the Christoffel equation for local medium parameters. These polarization vectors can be represented in the space domain as localized filtering operators, which resemble conventional derivative operators. The spatially variable pseudo-derivative operators perform well in heterogeneous VTI media even at places of rapid velocity/density variation. Synthetic results indicate that the operators can be used to separate wavefields for VTI media with an arbitrary degree of anisotropy.

### INTRODUCTION

Wave-equation migration for elastic data usually consists of two steps. The first step is reconstructing the subsurface wavefield from data recorded at the surface. The second step is applying an imaging condition that extracts reflectivity information from the reconstructed wavefields.

Elastic wave-equation migration for multicomponent data can be implemented in two ways. The first approach is to separate recorded elastic data into compressional and transverse (P- and S-) modes and

to use these separated modes for acoustic wave-equation migration. Acoustic imaging of elastic waves is used frequently, but it is based on the assumption that P and S data can be separated successfully on the surface, which is not always true (Etgen, 1988; Zhe and Greenhalgh, 1997). The second approach is not to separate P- and S-modes on the surface, extrapolate the entire elastic wavefield at once, then separate wave modes before applying an imaging condition. The elastic wavefields can be reconstructed using various techniques, including reverse time migration (RTM) (Chang and McMechan, 1986, 1994) and Kirchhoff-integral techniques (Hokstad, 2000).

The imaging condition applied to the reconstructed vector wavefields directly determines image quality. The conventional crosscorrelation imaging condition does not separate the wave modes and crosscorrelates the Cartesian components of the elastic wavefields. In general, P- and S-wave modes are mixed on all wavefield components and cause crosstalk and image artifacts. Yan and Sava (2008) suggest using imaging conditions based on elastic potentials, which require crosscorrelation of separated modes. Potential-based conditions create images that have clear physical meanings, in contrast with images obtained with Cartesian wavefield components, thus justifying the need for wave-mode separation.

As the need for anisotropic imaging increases, more processing and migration are performed based on anisotropic acoustic one-way wave equations (Alkhalifah, 1998, 2000; Shan and Biondi, 2005; Shan, 2006; Fletcher et al., 2008). However, much less research has been done on anisotropic elastic migration based on two-way wave equations. Elastic Kirchhoff migration (Hokstad, 2000) obtains pure-mode and converted-mode images by downward continuation of elastic vector wavefields with a viscoelastic wave equation. Wavefield separation is done effectively with elastic Kirchhoff integration, which handles P- and S-waves. However, Kirchhoff migration does not perform well in areas of complex geology where ray theory breaks down (Gray et al., 2001), thus requiring migration with more accurate methods, such as RTM.

One of the complexities that impedes elastic wave-equation anisotropic migration is the difficulty of separating anisotropic wavefields into different wave modes after reconstructing the elastic wavefields. However, proper separation of anisotropic wave modes is as important for anisotropic elastic migration as is the separation

Manuscript received by the Editor 19 November 2008; revised manuscript received 15 February 2009; published online 28 September 2009.

<sup>1</sup>Colorado School of Mines, Center for Wave Phenomena, Golden, Colorado, U.S.A. E-mail: jyan@mines.edu; psava@mines.edu.

© 2009 Society of Exploration Geophysicists. All rights reserved.

of isotropic wave modes for isotropic elastic migration. The main difference between anisotropic and isotropic wavefield separation is that Helmholtz decomposition is suitable only for separating isotropic wavefields and does not work well for anisotropic wavefields.

In this paper, we show how to construct wavefield separators for vertically transversely isotropic (VTI) media applicable to models with spatially varying parameters. We apply these operators to anisotropic elastic wavefields and show that they successfully separate anisotropic wave modes, even for extremely anisotropic media.

The main application of this technique is in the development of elastic RTM. In this case, complete wavefields containing P- and S-wave modes are reconstructed from recorded data. The reconstructed wavefields are separated in pure wave modes before applying a conventional crosscorrelation imaging condition. We limit the scope of our paper to the wave-mode separation procedure in highly heterogeneous media, although the ultimate goal is to aid elastic RTM.

## SEPARATION METHOD

Scalar and vector potentials can be separated by Helmholtz decomposition, which applies to any vector field  $\mathbf{W}(x, y, z)$ . By definition, the vector wavefield  $\mathbf{W}$  can be decomposed into a curl-free scalar potential  $\Theta$  and a divergence-free vector potential  $\Psi$  according to the relation (Aki and Richards, 2002)

$$\mathbf{W} = \nabla \Theta + \nabla \times \Psi. \quad (1)$$

Equation 1 is not used directly in practice, but the scalar and vector components are obtained indirectly by the applying the  $\nabla \cdot$  and  $\nabla \times$  operators to the extrapolated elastic wavefield:

$$P = \nabla \cdot \mathbf{W}, \quad (2)$$

$$\mathbf{S} = \nabla \times \mathbf{W}. \quad (3)$$

For isotropic elastic fields far from the source, quantities  $P$  and  $\mathbf{S}$  describe P- and S-wave modes, respectively (Aki and Richards, 2002).

Equations 2 and 3 allow us to understand why  $\nabla \cdot$  and  $\nabla \times$  pass compressional and transverse wave modes, respectively. In the discretized space domain, we can write

$$P = \nabla \cdot \mathbf{W} = D_x[W_x] + D_y[W_y] + D_z[W_z], \quad (4)$$

where  $D_x$ ,  $D_y$ , and  $D_z$  represent spatial derivatives in the  $x$ -,  $y$ -, and  $z$ -directions. Applying derivatives in the space domain is equivalent to applying finite-difference filtering to the functions. Here,  $D[\ ]$  represents spatial filtering of the wavefield with finite-difference operators. In the Fourier domain, we can represent the operators  $D_x$ ,  $D_y$ , and  $D_z$  by  $ik_x$ ,  $ik_y$ , and  $ik_z$ ; therefore, we can write an expression equivalent to expression 4 as

$$\tilde{P} = i\mathbf{k} \cdot \tilde{\mathbf{W}} = ik_x \tilde{W}_x + ik_y \tilde{W}_y + ik_z \tilde{W}_z, \quad (5)$$

where  $\mathbf{k} = \{k_x, k_y, k_z\}$  represents the wave vector and  $\tilde{\mathbf{W}}(k_x, k_y, k_z)$  is the 3D Fourier transform of the wavefield  $\mathbf{W}(x, y, z)$ .

In this domain, the operator  $i\mathbf{k}$  essentially projects the wavefield  $\tilde{\mathbf{W}}$  onto the wave vector  $\mathbf{k}$ , which represents the polarization direction for P-waves. Similarly, the operator  $\nabla \times$  projects the wavefield onto the direction orthogonal to  $\mathbf{k}$ , which represents the polarization direction for S-waves (Dellinger and Etgen, 1990). For illustration, Figure 1a shows the polarization vectors of the P-mode of a 2D isotropic model as a function of normalized  $k_x$  and  $k_z$  ranging from  $-1$  to  $1$  cycle. The polarization vectors are radial because the P-waves in an isotropic medium are polarized in the same directions as the wave vectors.

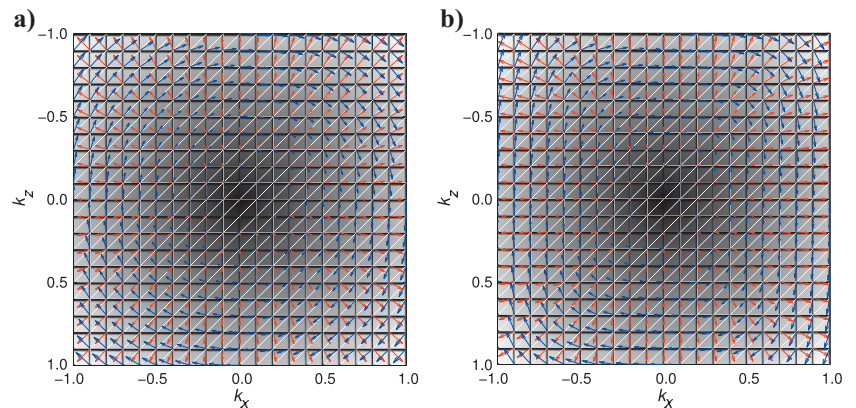
Dellinger and Etgen (1990) suggest the idea that wave-mode separation can be extended to anisotropic media by projecting the wavefields onto the directions in which the P- and S-modes are polarized. This requires that we modify the wave separation expression 5 by projecting the wavefields onto the true polarization directions  $\mathbf{U}$  to obtain quasi-P (qP-) waves:

$$\tilde{qP} = i\mathbf{U}(\mathbf{k}) \cdot \tilde{\mathbf{W}} = iU_x \tilde{W}_x + iU_y \tilde{W}_y + iU_z \tilde{W}_z. \quad (6)$$

In anisotropic media,  $\mathbf{U}(k_x, k_y, k_z)$  is different from  $\mathbf{k}$ , as illustrated in Figure 1b, which shows the polarization vectors of qP-wave mode for a 2D VTI anisotropic model with normalized  $k_x$  and  $k_z$  ranging from  $-1$  to  $1$  cycle. Polarization vectors are not radial because qP-waves in an anisotropic medium are not polarized in the same directions as wave vectors, except in the symmetry planes ( $k_z = 0$ ) and along the symmetry axis ( $k_x = 0$ ).

Dellinger and Etgen (1990) demonstrate wave-mode separation in the wavenumber domain using projection of the polarization vectors, as indicated in equation 6. However, for heterogeneous media, this equation does not work because the polarization vectors vary spatially. We can write an equivalent expression to equation 6 in the space domain for each grid point as

Figure 1. The qP- and qS-mode polarization vectors as a function of normalized wavenumbers  $k_x$  and  $k_z$  ranging from  $-1$  to  $1$  cycle for (a) an isotropic model with  $V_p = 3$  km/s and  $V_s = 1.5$  km/s, and (b) an anisotropic (VTI) model with  $V_{p0} = 3$  km/s,  $V_{s0} = 1.5$  km/s,  $\epsilon = 0.25$ , and  $\delta = -0.29$ . The red arrows are the qP-wave polarization vectors; the blue arrows are the qS-wave polarization vectors.



$$\mathbf{qP} = \nabla_a \cdot \mathbf{W} = L_x[W_x] + L_y[W_y] + L_z[W_z], \quad (7)$$

where  $L_x$ ,  $L_y$ , and  $L_z$  represent the inverse Fourier transforms of  $iU_x$ ,  $iU_y$ , and  $iU_z$  and where  $L[\ ]$  represents spatial filtering of the wavefield with anisotropic separators. The values  $L_x$ ,  $L_y$ , and  $L_z$  define the pseudo-derivative operators in the  $x$ -,  $y$ -, and  $z$ -directions for an anisotropic medium; they change from location to location according to the material parameters.

We obtain the polarization vectors  $\mathbf{U}(\mathbf{k})$  by solving the Christoffel equation (Aki and Richards, 2002; Tsvankin, 2005):

$$[\mathbf{G} - \rho V^2 \mathbf{I}] \mathbf{U} = 0, \quad (8)$$

where  $\mathbf{G}$  is the Christoffel matrix  $G_{ij} = c_{ijkl} n_j n_l$ , in which  $c_{ijkl}$  is the stiffness tensor, and where  $n_j$  and  $n_l$  are the normalized wave-vector components in the  $j$  and  $l$  directions,  $i, j, k, l = 1, 2, 3$ . The parameter  $V$  corresponds to the eigenvalues of the matrix  $\mathbf{G}$ . The eigenvalues  $V$  represent the phase velocities of different wave modes and are functions of  $\mathbf{k}$  (corresponding to  $n_j$  and  $n_l$  in  $\mathbf{G}$ ). For plane waves propagating in a VTI medium, we can set  $k_y$  to zero and get

$$\begin{bmatrix} c_{11}k_x^2 + c_{55}k_z^2 - \rho V^2 & 0 & (c_{13} + c_{55})k_x k_z \\ 0 & c_{66}k_x^2 + c_{55}k_z^2 - \rho V^2 & 0 \\ (c_{13} + c_{55})k_x k_z & 0 & c_{55}k_x^2 + c_{33}k_z^2 - \rho V^2 \end{bmatrix} \begin{bmatrix} U_x \\ U_y \\ U_z \end{bmatrix} = 0. \quad (9)$$

The middle row of this matrix characterizes the SH-wave polarized in the  $y$ -direction; the qP- and qSV-modes are uncoupled from the SH-mode and are polarized in the vertical plane. The top and bottom rows of this equation allow us to compute the polarization vector  $\mathbf{U} = \{U_x, U_z\}$  (the eigenvectors of the matrix) of the P- or SV-wave mode, given the stiffness tensor at every location of the medium.

We can extend the procedure to heterogeneous media by computing a different operator at every grid point. In the symmetry planes of VTI media, the 2D operators depend on the local values of the stiffness coefficients. For each point, we precompute the polarization vectors as a function of the local medium parameters and transform them to the space domain to obtain the wave-mode separators. We assume that the medium parameters vary smoothly (locally homogeneous); but even for complex media, the localized operators work in the same way as the long finite-difference operators. If we represent the stiffness coefficients using Thomsen parameters (Thomsen, 1986), then the pseudo-derivative operators  $L_x$  and  $L_z$  depend on  $\varepsilon$ ,  $\delta$ ,  $V_{p0}$ , and  $V_{s0}$ , which can be spatially varying parameters.

We can compute and store the operators for each grid point in the medium and then use those operators to separate P- and S-modes from reconstructed elastic wavefields at different time steps. Thus, wavefield separation in VTI media can be achieved by nonstationary filtering with operators  $L_x$  and  $L_z$ .

## OPERATOR PROPERTIES

In this section, we discuss the properties of the anisotropic derivative operators, including order of accuracy, size, and compactness.

### Operator orders

As we have shown, the isotropic separation operators (divergence and curl) in equations 4 and 5 are exact in the  $x$ - and  $k$ -domains. The exact derivative operators are infinitely long series in the discretized space domain. In practice, when evaluating the derivatives numerically, we must take some approximations to make the operators short and computationally efficient.

Usually, difference operators are evaluated at different orders of accuracy. The higher-order the approximation is, the more accurate and longer the operator becomes. For example, Figure 2a shows that the second-order operator has coefficients  $(-1/2, +1/2)$ , and the more accurate fourth-order operator has coefficients  $(+1/12, -2/3, 2/3, -1/12)$  (Fornberg and Ghrist, 1999).

In the wavenumber domain for isotropic media, as shown by the black line in Figure 2b, the exact difference operator is  $ik$ . Appendix A shows the  $k$ -domain equivalents of the second-, fourth-, sixth-, and eighth-order finite-difference operators; they are plotted in Figure 2b. The higher-order operators have responses closer to the exact operator  $ik$  (black line).

To obtain vertical and horizontal derivatives of different orders of accuracy, we weight the polarization vector  $i\mathbf{k}$  components  $ik_x$  and  $ik_z$  by the weights shown in Figure 2c. For VTI media, similarly, we weight the anisotropic polarization vector  $i\mathbf{U}(\mathbf{k})$  components  $iU_x$  and  $iU_z$  by these same weights. The weighted vectors are then transformed back to the space domain to obtain the anisotropic stencils.

### Operator size and compactness

Figure 3 shows the derivative operators of second, fourth, sixth, and eighth orders in the  $z$ - and  $x$ -directions for isotropic and VTI ( $\varepsilon = 0.25$ ,  $\delta = -0.29$ ) media. As we can see, isotropic operators

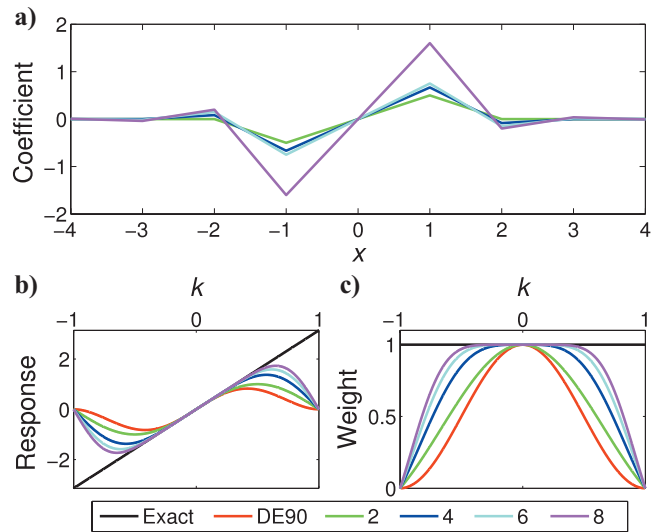


Figure 2. Comparison of derivative operators of different orders of accuracy (second, fourth, sixth, eighth order in space and the approximation applied in Dellinger and Etgen [1990] — cosine taper) in (a) the  $x$ -domain and (b) the  $k$ -domain. (c) Weights to apply to the components of the polarization vectors.

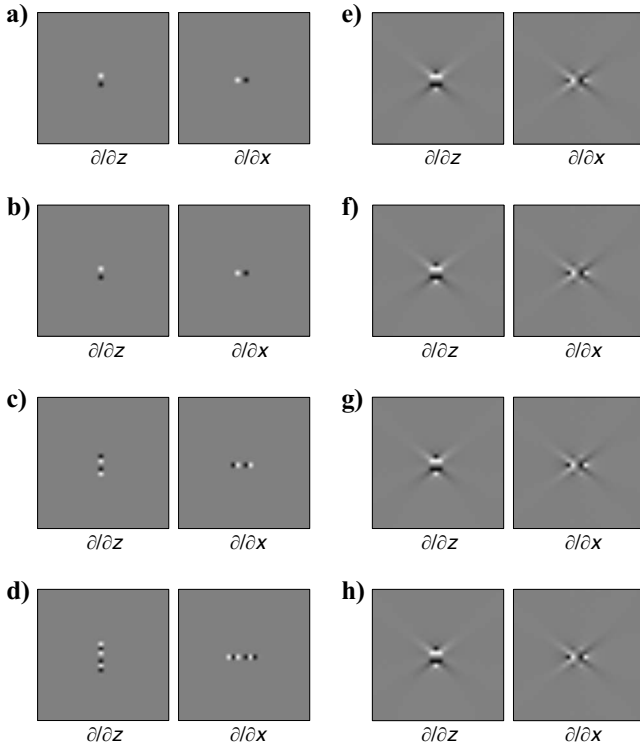


Figure 3. Second-, fourth-, sixth-, and eighth-order derivative operators for an isotropic medium ( $V_p = 3$  km/s and  $V_s = 1.5$  km/s) and a VTI medium ( $V_{p0} = 3$  km/s,  $V_{s0} = 1.5$  km/s,  $\varepsilon = 0.25$ , and  $\delta = -0.29$ ). (a-d) Isotropic operators; (e-h) anisotropic operators. From top to bottom are operators with increasing orders of accuracy.

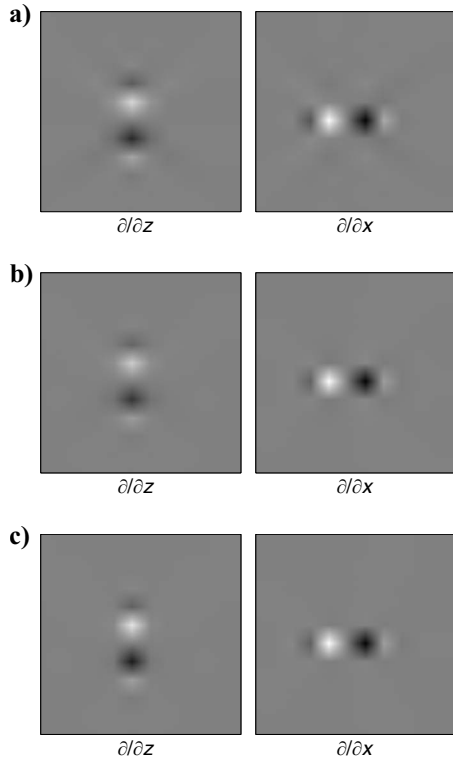


Figure 4. Eighth-order anisotropic pseudo-derivative operators for three VTI media: (a)  $\varepsilon = 0.25$ ,  $\delta = -0.29$ , (b)  $\varepsilon = 0.54$ ,  $\delta = 0$ ; and (c)  $\varepsilon = 0.2$ ,  $\delta = 0$ .

lengthen when the order of accuracy is higher. Anisotropic operators, however, change little in size. The central parts of the anisotropic operators look similar to their corresponding isotropic operators and change with the order of accuracy, although the outer parts of these anisotropic operators look the same and do not change with the order of accuracy. This indicates that the central parts of the operators are determined by the order of accuracy, and the outer parts represent the degree of anisotropy.

Figure 4 shows anisotropic derivative operators with the same order of accuracy (eighth order in space) for three VTI media with different combinations of  $\varepsilon$  and  $\delta$ . These operators have similar central parts but different outer parts. This result is consistent with the observation that the central part of an operator is determined by the order of accuracy and the outer part is controlled by anisotropy parameters.

Figure 5a shows the influence of approximation to finite difference (second and eighth orders, Figure 3h and e). The anisotropic part (diagonal tails) is almost the same, and the difference comes from the central part. Figure 5b shows the difference between operators with different anisotropy (Figure 4a and b). The difference mainly lies in the tails of the operators.

A comparison between Figure 4a and b shows that when we have a large difference between  $\varepsilon$  and  $\delta$ , the operator is big; when the difference between  $\varepsilon$  and  $\delta$  stays the same,  $\delta$  affects the operator size. A comparison between Figure 4b and c shows that when the difference between  $\varepsilon$  and  $\delta$  becomes smaller and  $\delta$  does not change, the operator gets smaller in size. This result is consistent with the polarization equation for VTI media with weak anisotropy (Tsvankin, 2005):

$$v_p = \theta + B[\delta + 2(\varepsilon - \delta)\sin^2 \theta]\sin 2\theta, \quad (10)$$

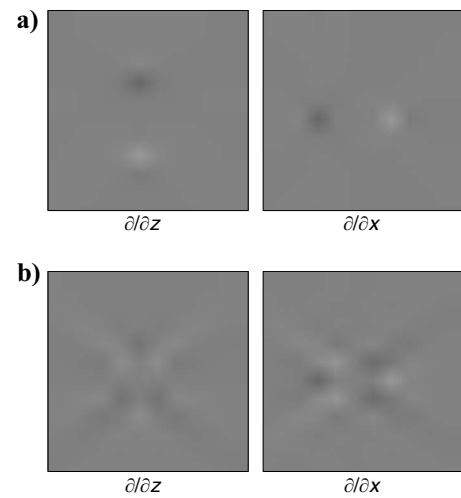


Figure 5. (a) Difference between the eighth- and second-order operators (Figure 3g and e) for a VTI medium with anisotropy  $\varepsilon = 0.25$ ,  $\delta = -0.29$  in the  $z$ - and  $x$ -directions. (b) Difference between the eighth-order anisotropic operators for a VTI medium with anisotropy  $\varepsilon = 0.25$ ,  $\delta = -0.29$  (Figure 4a) and a VTI medium with anisotropy  $\varepsilon = 0.54$ ,  $\delta = 0$  (Figure 4b).



where

$$B \equiv \frac{1}{2f} = \frac{1}{2 \left( 1 - \frac{V_{S0}^2}{V_{P0}^2} \right)}.$$

Here,  $V_{P0}$  and  $V_{S0}$  are vertical P- and S-wave velocities,  $\theta$  is the phase angle, and  $\nu_P$  is the P-wave polarization angle. Equation 10 demonstrates the deviation of anisotropic polarization vectors with the isotropic ones: the difference of  $\varepsilon$  and  $\delta$  (which is approximately  $\eta$  for weak anisotropy) and  $\delta$  control the deviation of  $\nu_P$  from  $\theta$  and therefore the size of the anisotropic derivative operators.

### Operator truncation

The derivative operators for isotropic and anisotropic media are very different in shape and size, and the operators vary with the strength of anisotropy. In theory, analytic isotropic derivatives are point operators in the continuous limit. If we can do a perfect Fourier transform to  $ik_x$  and  $ik_z$  (without doing the approximations to different orders of accuracy as in Figure 2), we get point derivative operators. This is because  $ik_x$  is constant in the  $z$ -direction (see Figure 6a), whose Fourier transform is a delta function; the exact expression of  $ik_x$  in the  $k$ -domain also points the operator in the  $x$ -direction. This

makes the isotropic derivative operators point operators in the  $x$ - and  $z$ -directions. When we apply approximations to the operators, they are compact in the space domain.

However, even if we do perfect Fourier transformation to  $iU_x$  and  $iU_z$  (without the approximations for different orders of accuracy) for VTI media, the operators will not be point operators because  $iU_x$  and  $iU_z$  are not constants in the  $z$ - and  $x$ -directions, respectively (see Figure 6b). The  $x$ -domain operators spread out in all directions (Figure 3e-h).

This effect is illustrated in Figure 3. When the order of accuracy decreases, the isotropic operators become more compact (shorter in space) but the anisotropic operators do not get more compact. No matter how we improve the compactness of isotropic operators, we do not get compact *anisotropic* operators in the space domain by the same means.

Because the size of the anisotropic derivative operators is usually large, it is natural that one would truncate the operators to save computation. Figure 7 shows a snapshot of an elastic wavefield and corresponding derivative operators for a VTI medium with  $\varepsilon = 0.25$  and  $\delta = -0.29$ . Figure 8 shows the attempt to separate using a truncated operator size of (a)  $11 \times 11$ , (b)  $31 \times 31$ , and (c)  $51 \times 51$  out of the full operator size  $65 \times 65$ . Figure 8 shows that the truncation leaves wave modes incompletely separated. This is because the truncation changes the direction of the polarization vectors, projecting

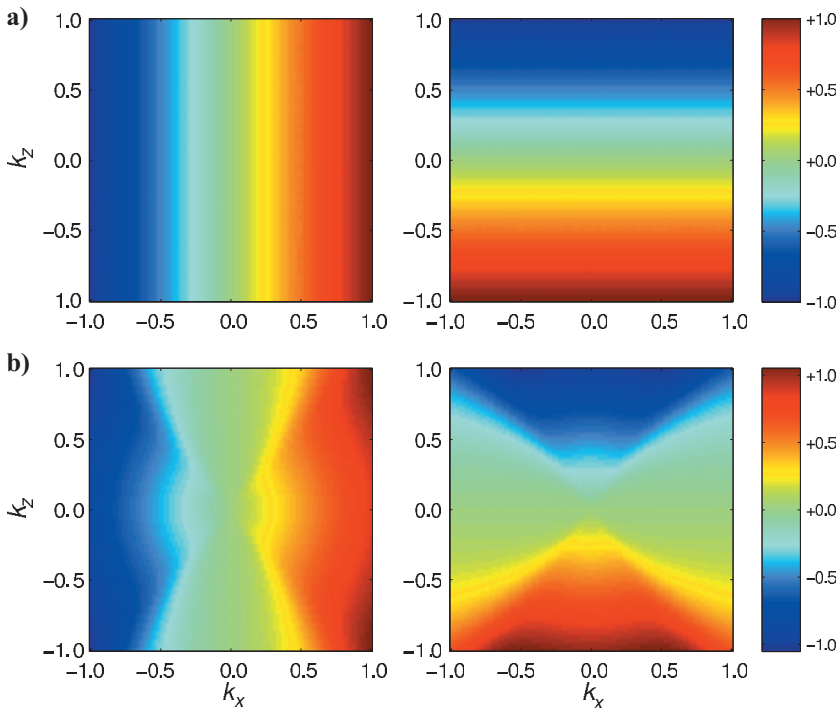


Figure 6. (a) Isotropic and (b) VTI ( $\varepsilon = 0.25$ ,  $\delta = -0.29$ ) polarization vectors (Figure 2) projected onto the  $x$ - (left column) and  $z$ -directions (right column). The isotropic polarization vectors' components in the  $z$ - and  $x$ -directions depend only on  $k_z$  and  $k_x$ , respectively. In contrast, the anisotropic polarization vectors' components are functions of  $k_x$  and  $k_z$ .

the wavefield displacement onto the wrong direction.

A comparison of the deviation of polarization vectors before and after truncation is plotted in Figure 9. For the operator size of  $11 \times 11$ , the polarization vectors only deviate from the correct ones to a maximum of  $10^\circ$ ; however, even this difference makes the separation incomplete.

## EXAMPLES

We illustrate the anisotropic wave-mode separation with a simple synthetic example and a more challenging elastic Sigsbee 2A model (Paffenholz et al., 2002).

### Simple model

We consider a 2D isotropic model characterized by the  $V_P$ ,  $V_S$ , and density shown in Figure 10a-c. The model contains negative P- and S-wave velocity anomalies that triplicate the wavefields. The source is located at the center of the model. Figure 11a shows the vertical and horizontal components of one snapshot of the simulated elastic wavefield (generated using the eighth-order finite-difference solu-

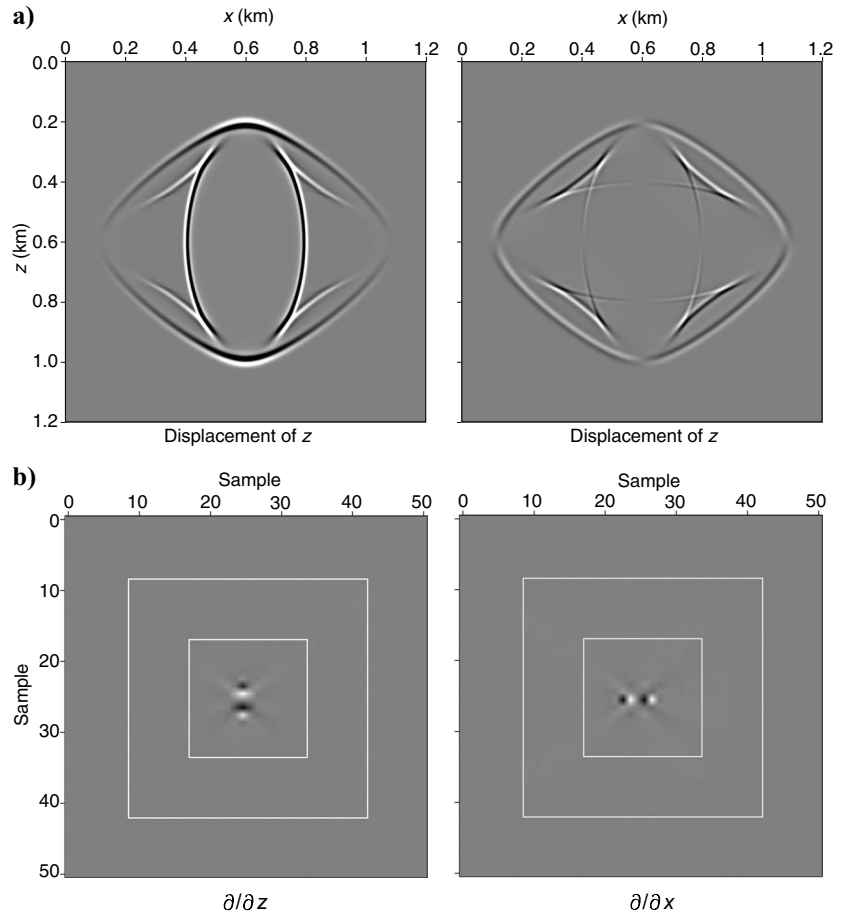
tion of the elastic wave equation), Figure 11b shows the separation to P- and S-modes using  $\nabla \cdot$  and  $\nabla \times$  operators, and Figure 11c shows the mode separation obtained using the pseudo-derivative operators on the medium parameters. A comparison of Figure 11b and c indicates that the  $\nabla \cdot$  and  $\nabla \times$  operators and the pseudo-derivative operators work identically well for this isotropic medium.

We consider a 2D anisotropic model similar to the model shown in Figure 10a-c, characterized by  $\varepsilon$  and  $\delta$  shown in Figure 10d and e. The parameters  $\varepsilon$  and  $\delta$  vary gradually from top to bottom and left to right, respectively. The upper-left part of the medium is isotropic, and the lower-right part is highly anisotropic. Because the difference of  $\varepsilon$  and  $\delta$  is great at the bottom part of the model, the qS-waves in that region are triplicated severely as a result of the strong anisotropy.

Figure 12 illustrates the pseudo-derivative operators obtained at different locations in the model defined by the intersections of  $x$ -coordinates 0.3, 0.6, 0.9 km and  $z$ -coordinates 0.3, 0.6, 0.9 km. Because the operators correspond to different combinations of  $\varepsilon$  and  $\delta$ , they have different forms. The isotropic operator at  $x = 0.3$  km and  $z = 0.3$  km (Figure 12a) is purely vertical and horizontal, whereas the anisotropic operators (Figure 12b-i) have tails radiating from the center. The operators get larger at locations where the medium is more anisotropic, e.g., at  $x = 0.9$  km and  $z = 0.9$  km.

Figure 13a shows the vertical and horizontal components of one snapshot of the simulated elastic anisotropic wavefield, Figure 13b

Figure 7. (a) A snapshot of an elastic wavefield showing the vertical (left) and horizontal (right) components for a VTI medium ( $\varepsilon = 0.25$  and  $\delta = -0.29$ ). (b) Eighth-order anisotropic pseudo-derivative operators in the  $z$ -(left) and  $x$ -(right) directions for this VTI medium. The boxes show the truncation of the operator to sizes of  $11 \times 11$ ,  $31 \times 31$ , and  $51 \times 51$ .



shows the separation to qP- and qS-modes using conventional isotropic  $\nabla \cdot$  and  $\nabla \times$  operators, and Figure 13c shows the mode separation obtained using the pseudooperators constructed with the local medium parameters. A comparison of Figure 13b and c) indicates that the spatially varying derivative operators successfully separate the elastic wavefields into qP- and qS-modes, but the  $\nabla \cdot$  and  $\nabla \times$  operators only work in the isotropic region of the model.

### Sigsbee model

Our second model (Figure 14) uses an elastic anisotropic version of the Sigsbee 2A model (Paffenholz et al., 2002). In our modification, the P-wave velocity is taken from the original model,  $V_p/V_s$  ranges from 1.5 to 2,  $\varepsilon$  ranges from 0 to 0.48 (Figure 14d), and  $\delta$  ranges from 0 to 0.10 (Figure 14e). The model is isotropic in the salt and the top part of the model. A vertical point-force source is located

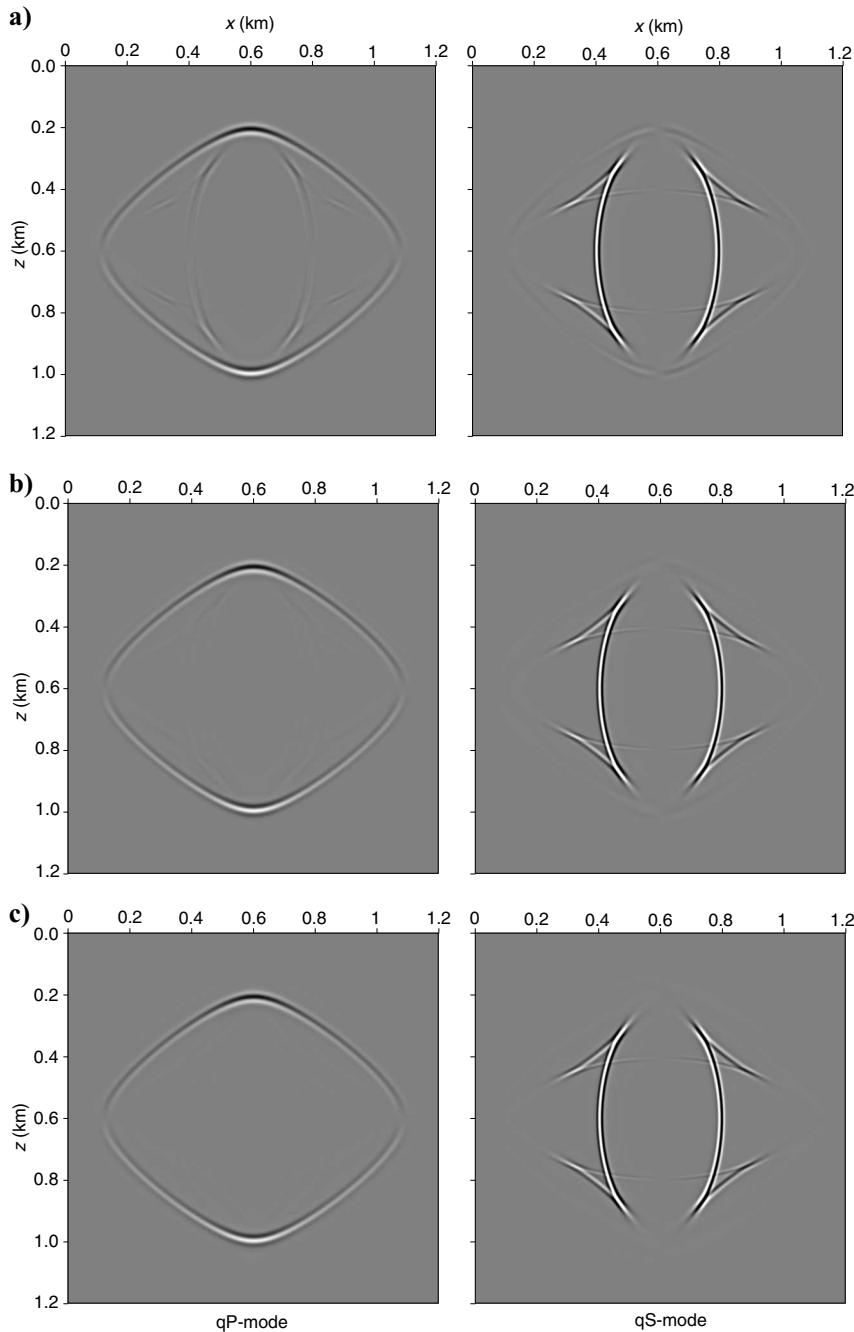


Figure 8. Separation by eighth-order anisotropic pseudo-derivative operators of different sizes: (a)  $11 \times 11$ , (b)  $31 \times 31$ , (c)  $51 \times 51$ , shown in Figure 7b. The larger the operators, the better the separation.

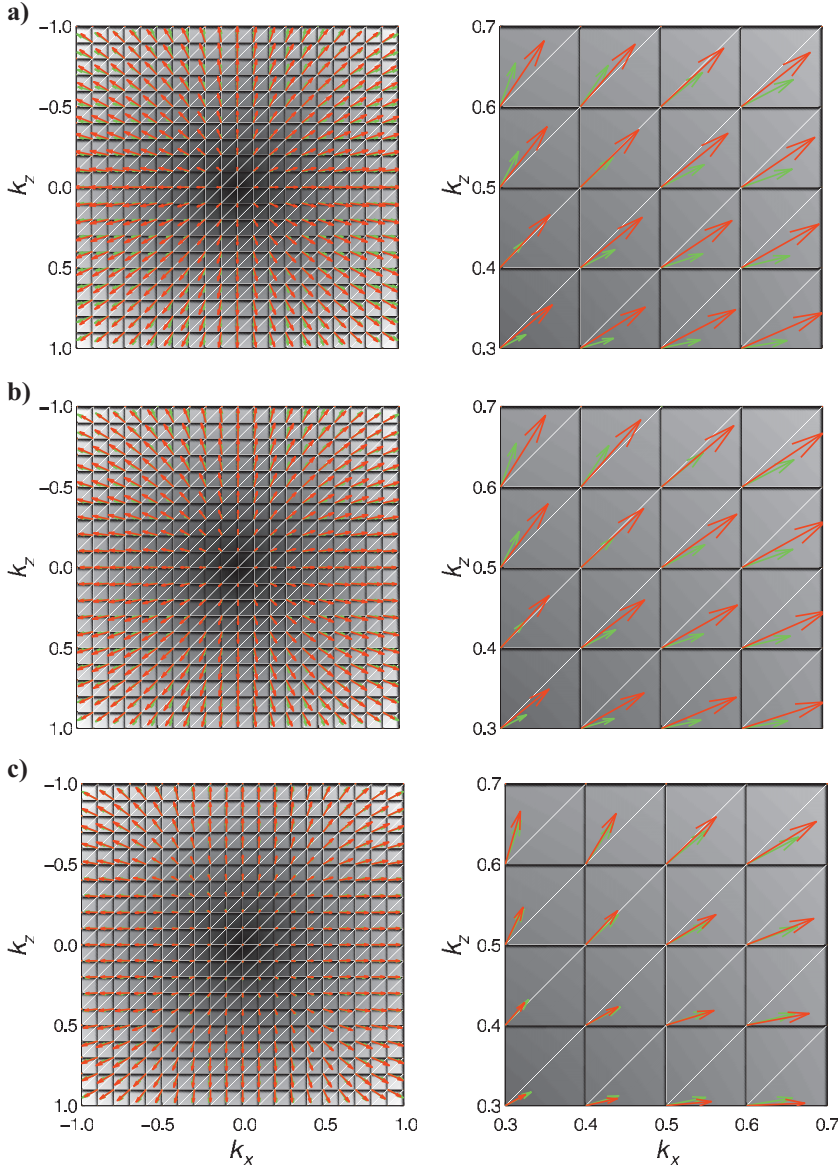


Figure 9. Deviation of polarization vectors by truncating the operator size to (a)  $11 \times 11$ , (b)  $31 \times 31$ , and (c)  $51 \times 51$  out of  $65 \times 65$ . The left column shows polarization vectors from  $-1$  to  $1$  cycle in the  $x$ - and  $z$ -directions; the right column zooms from  $0.3$  to  $0.7$  cycles. The green vectors are the exact polarization vectors; the red ones are the effective polarization vectors after truncation of the operator in the  $x$ -domain.

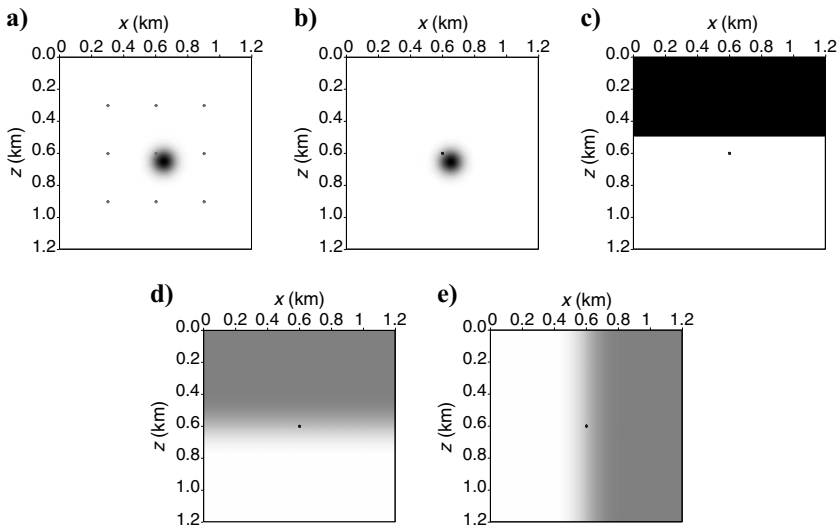


Figure 10. A  $1.2 \times 1.2$ -km model with parameters (a)  $V_{p0} = 3$  km/s except for a low-velocity Gaussian anomaly at  $x = 0.65$  km and  $z = 0.65$  km, (b)  $V_{s0} = 1.5$  km/s except for a low-velocity Gaussian anomaly at  $x = 0.65$  km and  $z = 0.65$  km, (c)  $\rho = 1$  g/cm<sup>3</sup> in the top layer and  $2$  g/cm<sup>3</sup> in the bottom layer, (d)  $\epsilon$  smoothly varying from  $0$  to  $0.25$  from top to bottom, (e)  $\delta$  smoothly varying from  $0$  to  $-0.29$  from left to right. A vertical point force source is located at  $x = 0.6$  km and  $z = 0.6$  km, shown by the dot in (b-e). The dots in (a) correspond to the locations of the anisotropic operators shown in Figure 12.



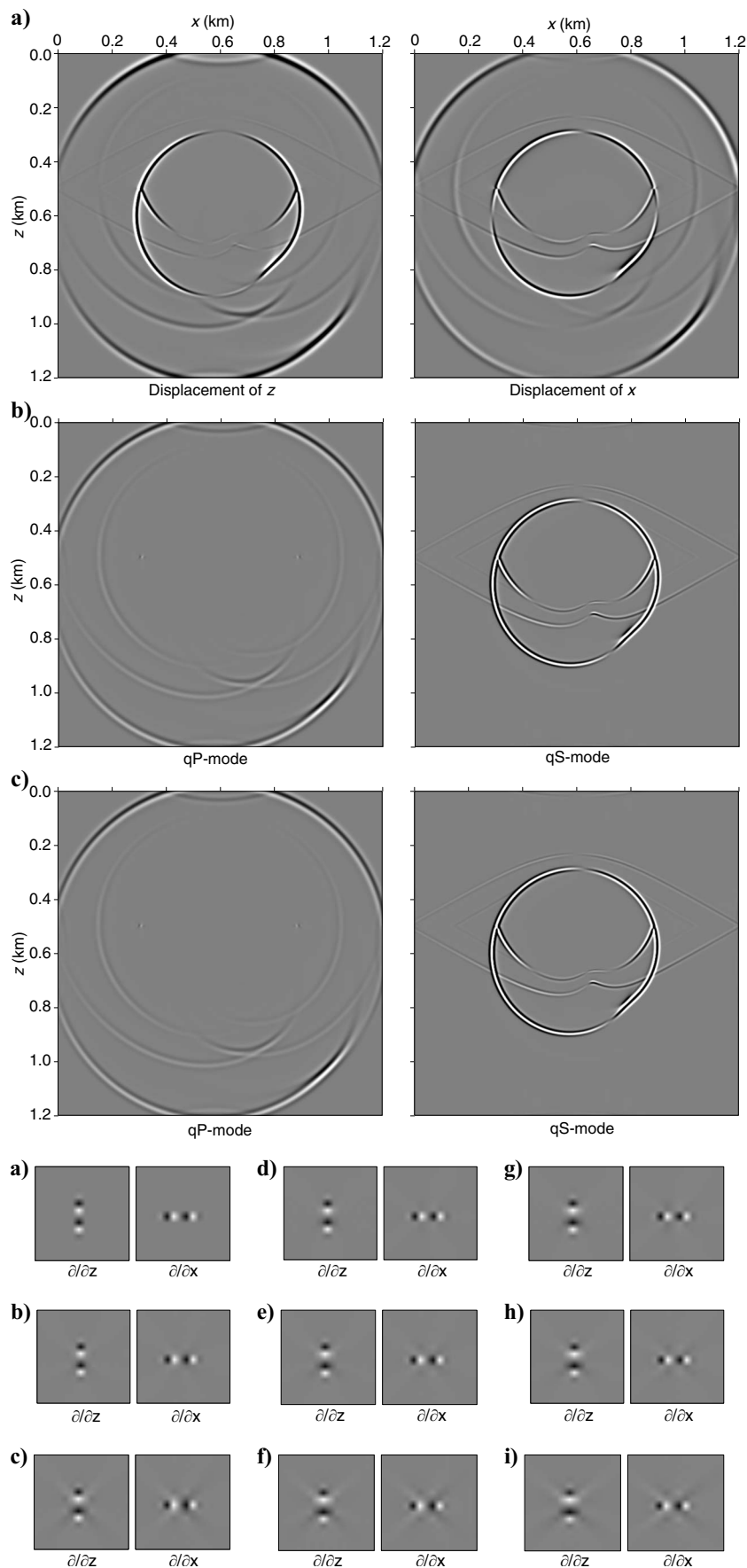


Figure 11. (a) A snapshot of the isotropic wavefield modeled with a vertical point-force source at  $x = 0.6$  km and  $z = 0.6$  km for the model shown in Figure 10a-c). (b) Isotropic P- and S-wave modes separated using  $\nabla \cdot$  and  $\nabla \times$ . (c) Isotropic P- and S-wave modes separated using pseudo-derivative operators. Both (b) and (c) show good separation results.

Figure 12. The eighth-order anisotropic pseudo-derivative operators in the z- and x-directions at the intersections of  $x = 0.3, 0.6, 0.9$  km, and  $z = 0.3, 0.6, 0.9$  km, for the model in Figure 10.

at  $x = 14.5$  km and  $z = 5.3$  km to simulate the elastic anisotropic wavefield.

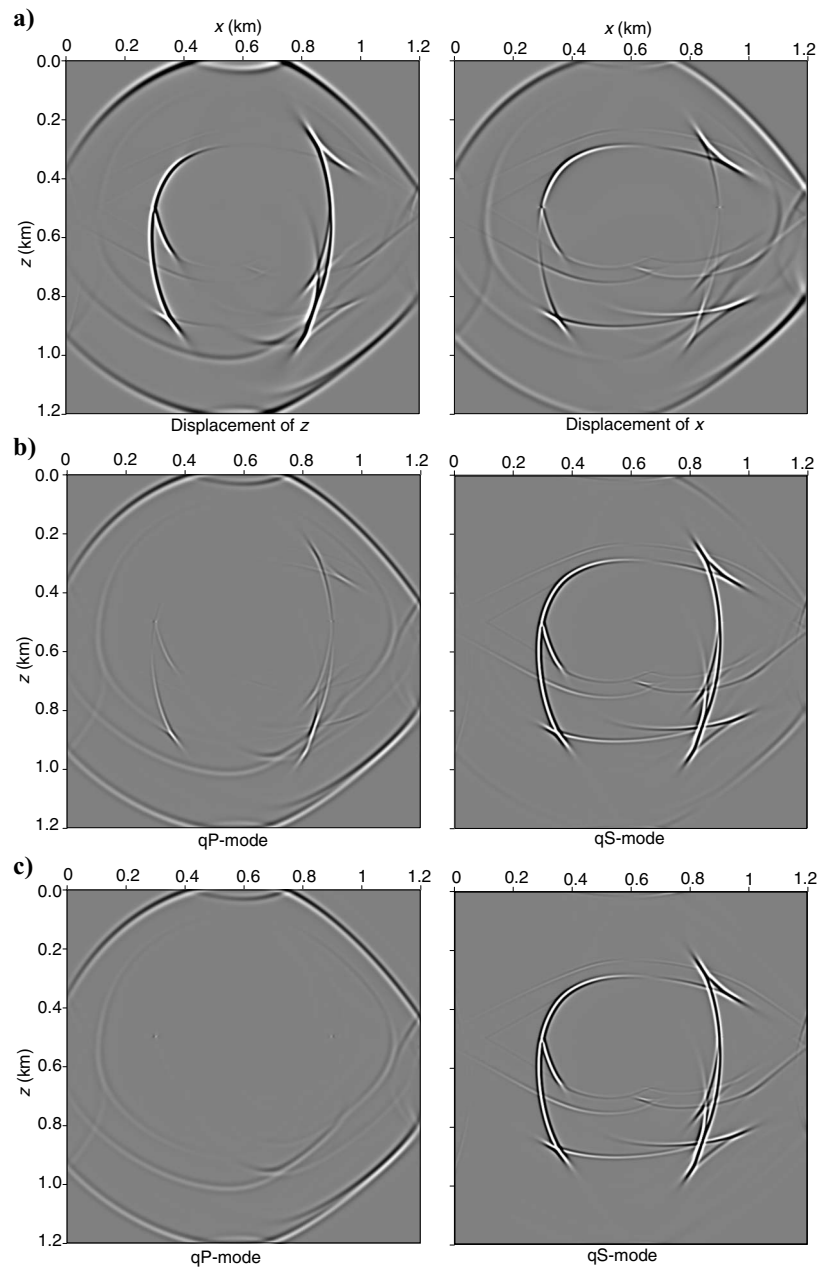
Figure 15 shows one snapshot of the modeled elastic anisotropic wavefields using the model in Figure 14. Figure 16 illustrates the separation of the anisotropic elastic wavefields using the  $\nabla \cdot$  and  $\nabla \times$  operators. Figure 17 illustrates the separation using our pseudo-derivative operators. Figure 16 shows the residual of unseparated P- and S-wave modes, such as at  $x = 13$  km and  $z = 7$  km in the qP-mode panel and at  $x = 11$  km and  $z = 7$  km in the qS-mode panel.

The residual of S-waves in the qP-mode panel of Figure 16 is very significant because of strong reflections from the salt bottom. This extensive residual can be harmful to subsalt elastic or even acoustic migration if not removed completely. In contrast, Figure 17 shows

the qP- and qS-modes better separated, demonstrating the effectiveness of the anisotropic pseudo-derivative operators constructed using the local medium parameters. These wavefields composed of well-separated qP- and qS-modes are essential to produce clean seismic images.

To test the separation with a homogeneous assumption of anisotropy in the model, we show in Figure 18 the separation with  $\varepsilon = 0.3$  and  $\delta = 0.1$  in the  $k$ -domain. This separation assumes a model with homogeneous anisotropy. The separation shows that residual remains in the separated panels. Although the residual is much weaker compared to separating using a isotropic model, it is still visible at locations such as at  $x = 13$  km and  $z = 7$  km, and  $x = 13$  km and  $z = 4$  km, in the qP-panel and at  $x = 16$  km and  $z = 2.5$  km in the qS-panel.

Figure 13. (a) A snapshot of the anisotropic wavefield modeled with a vertical point-force source at  $x = 0.6$  km and  $z = 0.6$  km for the model shown in Figure 10. (b) Anisotropic qP- and qS-modes separated using  $\nabla \cdot$  and  $\nabla \times$ . (c) Anisotropic qP- and qS-modes separated using pseudo-derivative operators. The separation of wavefields into qP- and qS-modes in (b) is incomplete, which is obvious at places such as at  $x = 0.4$  km,  $z = 0.9$  km. In contrast, the separation in (c) is much better because the correct anisotropic derivative operators are used.



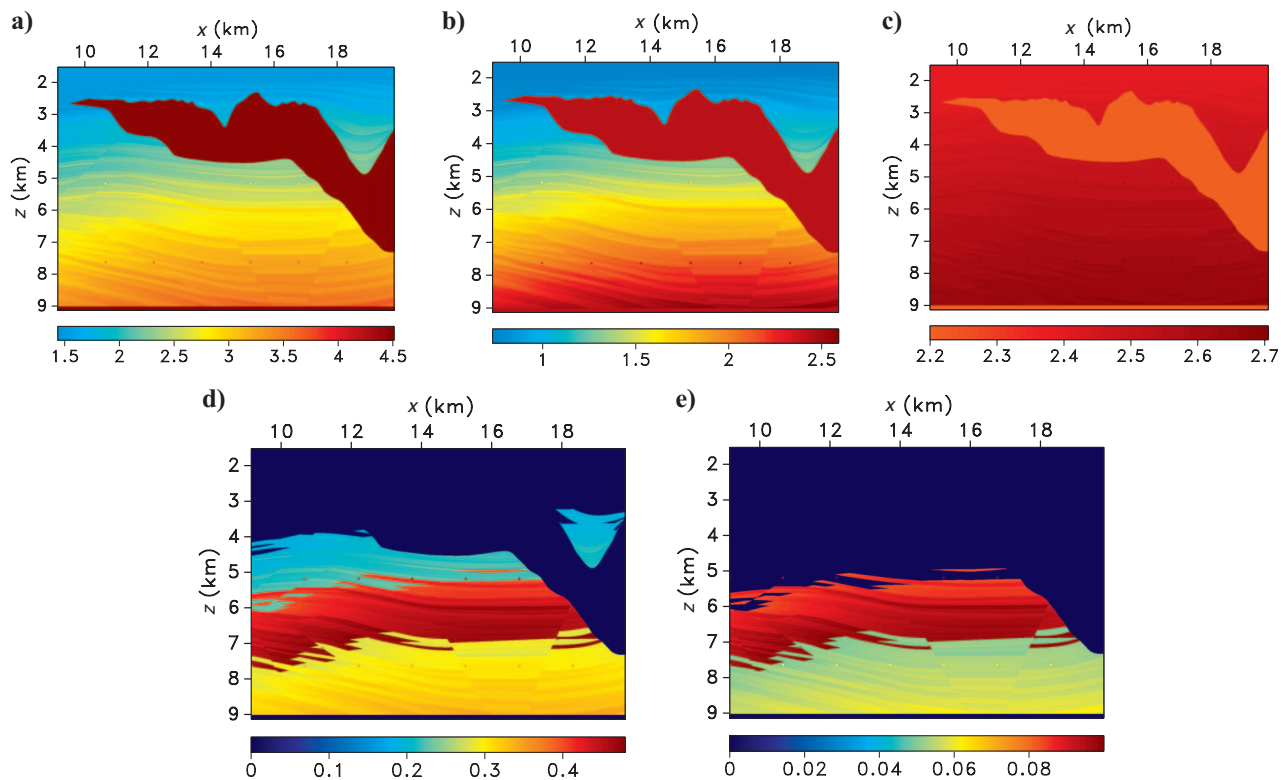


Figure 14. A Sigsbee 2A model in which (a) is the P-wave velocity (taken from the original Sigsbee 2A model [Paffenholz et al., 2002]), (b) is the S-wave velocity, where  $V_p/V_s$  ranges from 1.5 to 2, (c) is the density ranging from 2.2 to 2.7 g/cm<sup>3</sup>, (d) is  $\epsilon$  ranging from 0.2 to 0.48, and (e) is  $\delta$  ranging from 0 to 0.10 in the rest of the model.

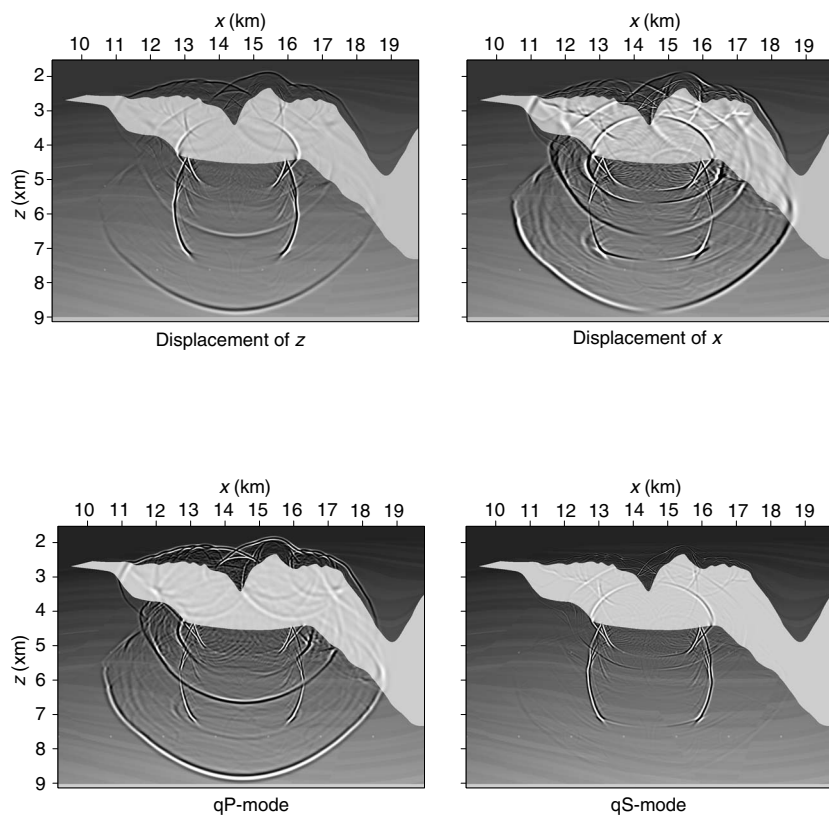


Figure 15. Anisotropic wavefield modeled with a vertical point force source at  $x = 14.3$  km and  $z = 5.3$  km for the model shown in Figure 14.

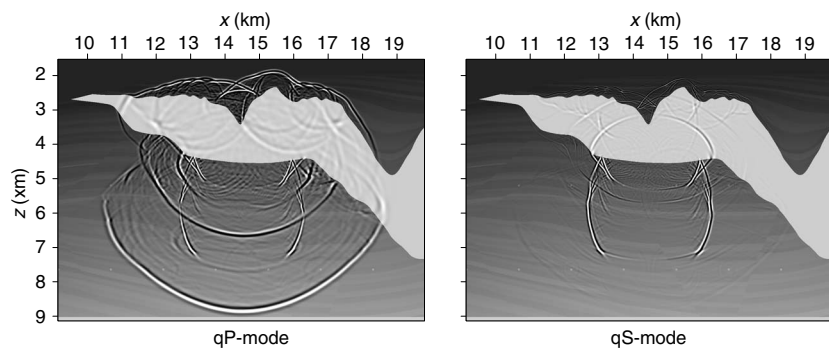


Figure 16. Anisotropic qP- and qS-modes separated using  $\nabla \cdot$  and  $\nabla \times$  for the vertical and horizontal components of the elastic wavefields shown in Figure 15. Residuals are obvious at places such as  $x = 13$  km and  $z = 7$  km in the qP-mode panel and at  $x = 11$  km and  $z = 7$  km in the qS-mode panel.

## DISCUSSION

The separation of P- and S-wave modes is based on the projection of elastic wavefields onto their respective polarization vectors. For VTI media, P- and S-mode polarization vectors can be obtained conveniently by solving the Christoffel equation. The Christoffel equation is a plane-wave solution to the elastic wave equation. Because the displacements, velocity, and anisotropy field have the same form of elastic wave equation, the separation algorithm applies to all of these wavefields. The P- and SV-mode separation can be extended to transverse isotropy with a tilted symmetry axis (TTI) media by solving a TTI Christoffel matrix and obtaining TTI separators. Physically, the TTI medium is a rotation of VTI media.

In TI media, SV- and SH-waves are uncoupled most of the time, where the SH-wave is polarized out of plane. We only need to decompose P- and SV-modes in the vertical plane. The plane-wave solution is sufficient for most TI media, except for a special case where there exists a singularity point at an oblique propagation angle in the vertical plane (a 3D line singularity), at which angle SV- and SH-wave velocities coincide.

At this point, the SV-wave polarization is not defined uniquely by the Christoffel equation. S-waves at the singularity are polarized in a plane orthogonal to the P-wave polarization vector. However, this is not a problem because we define SV-waves polarized in vertical planes only, removing the singularity by using the cylindrical coordinates. This situation is similar to S-wave-mode coupling in orthorhombic media, where there is at least one singularity in a quadrant. However, as pointed out by [Dellinger and Etgen \(1990\)](#), the singularity in orthorhombic media is a global property of the media and cannot be removed; therefore, the separation using polarization vectors to 3D orthorhombic is not straightforward.

The anisotropic derivative operators depend on the anisotropic medium parameters. In Figure 19, we show how sensitive the separation is to the medium parameters. The elastic-wavefield snapshot we use is shown in Figure 7a for a VTI medium with  $V_p/V_s = 2$  and  $\varepsilon = 0.25$ ,  $\delta = -0.29$ . We try to separate the P- and SV-modes with (a)  $\varepsilon = 0.4$ ,  $\delta = -0.1$ , (b)  $\varepsilon = 0$ ,  $\delta = -0.3$ , and (c)  $\varepsilon = 0$ ,  $\delta = 0$ . The separation shows that parameters (a) have good separation, showing the difference in  $\varepsilon$  and  $\delta$  is important. The worst-case scenario is shown by parameters (c), where isotropy is assumed for this VTI medium.

Figure 17. Anisotropic qP- and qS-modes separated using pseudo-derivative operators for the vertical and horizontal components of the elastic wavefields shown in Figure 15. They show better separation of qP- and qS-modes.

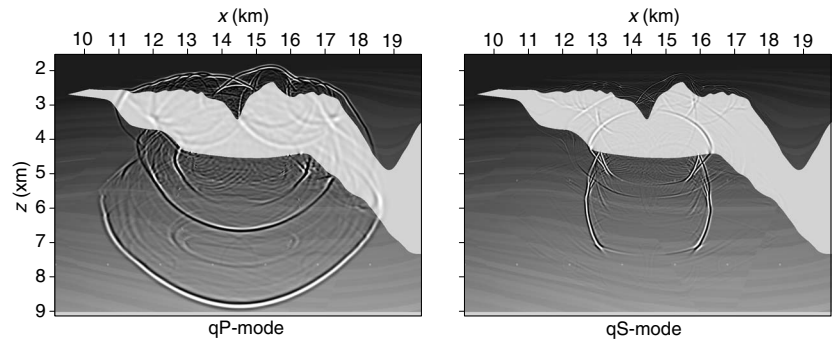
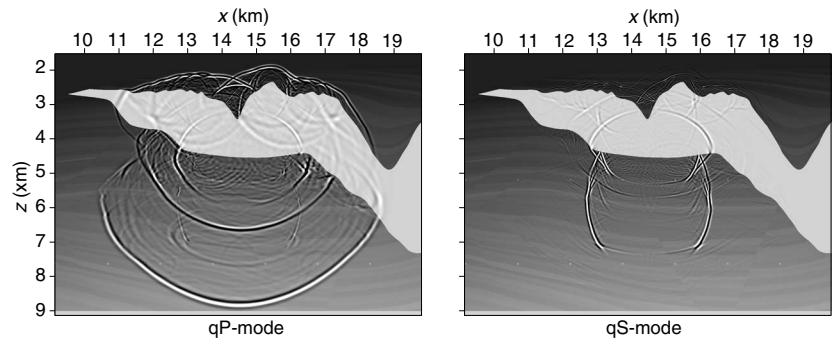


Figure 18. Anisotropic qP- and qS-modes separated in the  $k$ -domain for the vertical and horizontal components of the elastic wavefields shown in Figure 15. The separation assumes  $\varepsilon = 0.3$  and  $\delta = 0.1$  throughout the model. The separation is incomplete. Residuals are still visible at places such as at  $x = 13$  km and  $z = 7$  km, and at  $x = 13$  km and,  $z = 4$  km in the qP-mode panel and at  $x = 16$  km and  $z = 2.5$  km in the qS-mode panel.



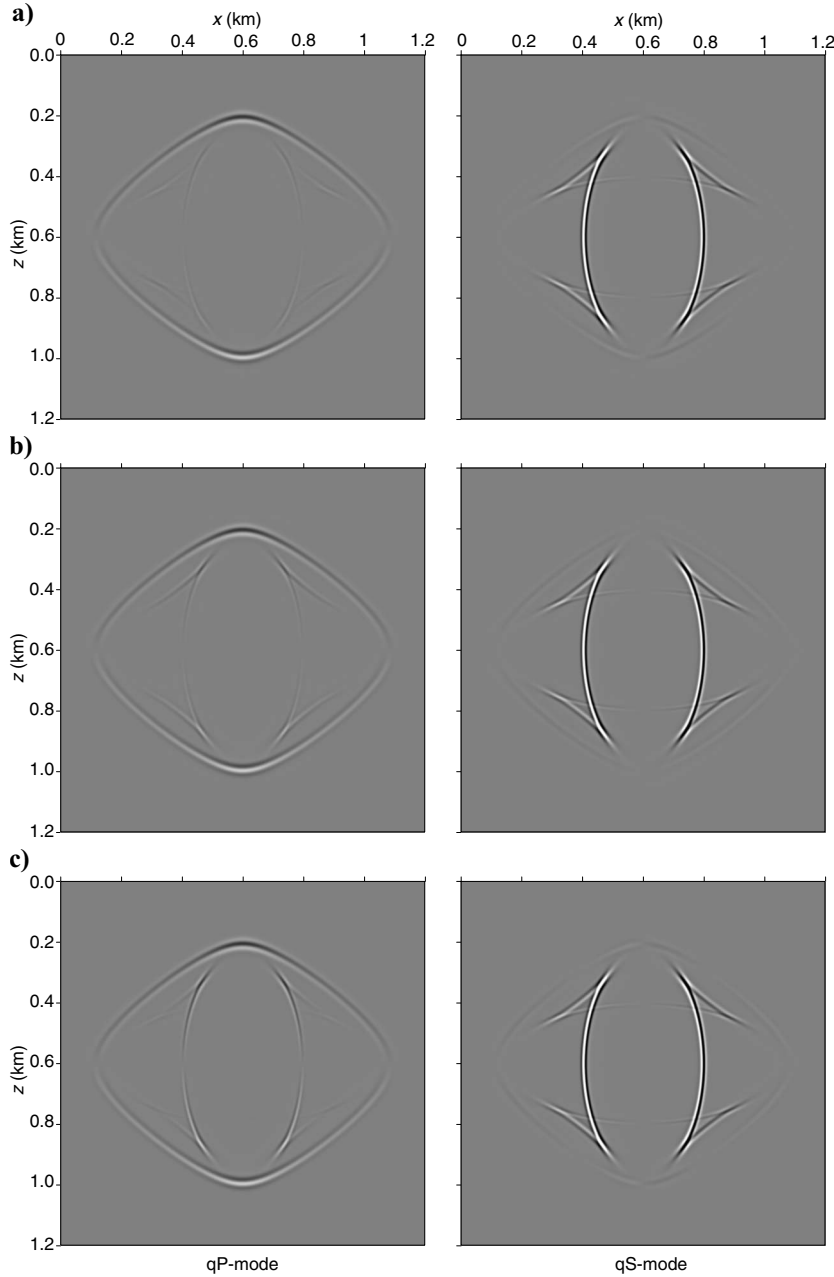


Figure 19. P- and SV-wave-mode separation for a snapshot shown in Figure 7a. The true medium parameters are  $\varepsilon = 0.25$ ,  $\delta = -0.29$ . The separation assumes medium parameters of (a)  $\varepsilon = 0.4$ ,  $\delta = -0.1$ , (b)  $\varepsilon = 0$ ,  $\delta = -0.3$ , and (c)  $\varepsilon = 0$ ,  $\delta = 0$ . Hard clipping was applied to show the weak events. The plot shows that the different estimate of anisotropy parameters influences wave-mode separation.

## CONCLUSIONS

We have presented a method of obtaining spatially varying pseudo-derivative operators with application to wave-mode separation in anisotropic media. The main idea is to utilize polarization vectors constructed in the wavenumber domain using the local medium parameters and then transform these vectors back to the space domain. The main advantage of applying the pseudo-derivative operators in the space domain constructed in this way is that they are suitable for heterogeneous media. The wave-mode separators obtained with this method are spatially variable filtering operators that can be used to

separate wavefields in VTI media with an arbitrary degree of anisotropy. This methodology is applicable for elastic RTM in heterogeneous anisotropic media.

## ACKNOWLEDGMENTS

We acknowledge the support of the sponsors of the Center for Wave Phenomena at Colorado School of Mines.

## APPENDIX A

### FINITE-DIFFERENCE APPROXIMATIONS TO DIFFERENT ORDERS OF ACCURACY

This appendix summarizes the wavenumber-domain weighting of the ideal derivative function  $ik_j$ ,  $j = 1, 2, 3$  for operators of various degrees of accuracy. Starting from the coefficients of a derivative stencil in the space domain, we can use conventional Z-transforms to construct a wavenumber-domain weighting function representing the same order of accuracy. We apply the weighting functions to the isotropic and anisotropic projections of the polarization vectors to obtain space-domain derivative operators of a similar order of accuracy.

For the case of second-order centered derivatives, the stencil has the following Z-transform representation:

$$D_2(Z) = -\frac{1}{2}(Z^1 - Z^{-1}). \quad (\text{A-1})$$

Transforming from Z to the wavenumber domain, we obtain

$$D_2(k) = -\frac{1}{2}(e^{ik} - e^{-ik}), \quad (\text{A-2})$$

which enables us to define the second-order weight

$$W_2(k) = \frac{\sin(k)}{k}. \quad (\text{A-3})$$

Here, the wavenumber  $k$  is normalized and hence is dimensionless.

Similarly, we can construct weights for fourth-, sixth-, and eighth-order operators from Z-transform representations:

$$D_4(Z) = -\frac{2}{3}(Z^1 - Z^{-1}) + \frac{1}{12}(Z^2 - Z^{-2}), \quad (\text{A-4})$$

$$D_6(Z) = -\frac{3}{4}(Z^1 - Z^{-1}) + \frac{3}{20}(Z^2 - Z^{-2}) - \frac{1}{60}(Z^3 - Z^{-3}), \quad (\text{A-5})$$



$$D_8(Z) = -\frac{4}{5}(Z^1 - Z^{-1}) + \frac{1}{5}(Z^2 - Z^{-2}) - \frac{4}{105}(Z^3 - Z^{-3}) + \frac{1}{140}(Z^4 - Z^{-4}), \quad (\text{A-6})$$

which transform to the wavenumber-domain weights:

$$D_4(k) = -\frac{2}{3}(e^{ik} - e^{-ik}) + \frac{1}{12}(e^{2ik} - e^{-2ik}), \quad (\text{A-7})$$

$$D_6(k) = -\frac{3}{4}(e^{ik} - e^{-ik}) + \frac{3}{20}(e^{2ik} - e^{-2ik}) - \frac{1}{60}(e^{3ik} - e^{-3ik}), \quad (\text{A-8})$$

$$D_8(k) = -\frac{4}{5}(e^{ik} - e^{-ik}) + \frac{1}{5}(e^{2ik} - e^{-2ik}) - \frac{4}{105}(e^{3ik} - e^{-3ik}) + \frac{1}{280}(e^{4ik} - e^{-4ik}). \quad (\text{A-9})$$

These lead to the following weighting functions:

$$W_4(k) = -\frac{4 \sin(k)}{3k} + \frac{\sin(2k)}{6k}, \quad (\text{A-10})$$

$$W_6(k) = -\frac{3 \sin(k)}{2k} + \frac{3 \sin(2k)}{10k} - \frac{\sin(3k)}{30k}, \quad (\text{A-11})$$

$$W_8(k) = -\frac{8 \sin(k)}{5k} + \frac{2 \sin(2k)}{5k} - \frac{8 \sin(3k)}{105k} + \frac{\sin(4k)}{140k}. \quad (\text{A-12})$$

The derivatives are shown in Figure 2a and b in the space and wavenumber domains, respectively. Comparing these weights and

their corresponding frequency responses, we see that we need to use higher-order difference operators to have better approximations to high frequencies. For comparison, the weight used in Dellinger and Etgen (1990) is  $1/2[1 + \cos(k)]$ . The cosine taper attenuates middle frequencies compared to high-order finite-difference operators.

## REFERENCES

- Aki, K., and P. Richards, 2002, Quantitative seismology, 2nd ed.: University Science Books.
- Alkhalifah, T., 1998, Acoustic approximations for processing in transversely isotropic media: *Geophysics*, **63**, 623–631.
- , 2000, An acoustic wave equation for anisotropic media: *Geophysics*, **65**, 1239–1250.
- Chang, W. F., and G. A. McMechan, 1986, Reverse-time migration of offset vertical seismic profiling data using the excitation-time imaging condition: *Geophysics*, **51**, 67–84.
- , 1994, 3-D elastic prestack, reverse-time depth migration: *Geophysics*, **59**, 597–609.
- Dellinger, J., and J. Etgen, 1990, Wave-field separation in two-dimensional anisotropic media: *Geophysics*, **55**, 914–919.
- Etgen, J. T., 1988, Prestacked migration of P- and SV-waves: 58th Annual International Meeting, SEG, Expanded Abstracts, 972–975.
- Fletcher, R., X. Du, and P. J. Fowler, 2008, A new pseudo-acoustic wave equation for TI media: 78th Annual International Meeting, SEG, Expanded Abstracts, 2082–2086.
- Fornberg, B., and M. Ghrist, 1999, Spatial finite difference approximations for wave-type equations: *SIAM Journal on Numerical Analysis*, **37**, 105–130.
- Gray, S. H., J. Etgen, J. Dellinger, and D. Whitmore, 2001, Seismic migration problems and solutions: *Geophysics*, **66**, 1622–1640.
- Hokstad, K., 2000, Multicomponent Kirchhoff migration: *Geophysics*, **65**, 861–873.
- Paffenholz, J., B. McLain, J. Zaske, and P. Keliher, 2002, Subsalt multiple attenuation and imaging: Observations from the Sigsbee2B synthetic data set: 72nd Annual International Meeting, SEG, Expanded Abstracts, 2122–2125.
- Shan, G., 2006, Optimized implicit finite-difference migration for VTI media: 76th Annual International Meeting, SEG, Expanded Abstracts, 2367–2371.
- Shan, G., and B. Biondi, 2005, 3D wavefield extrapolation in laterally varying tilted TI media: 75th SEG Annual International Meeting, SEG, Expanded Abstracts, 104–107.
- Thomsen, L., 1986, Weak elastic anisotropy: *Geophysics*, **51**, 1954–1966.
- Tsvankin, I., 2005, Seismic signatures and analysis of reflection data in anisotropic media, 2nd ed.: Elsevier Science Publ. Co., Inc.
- Yan, J., and P. Sava, 2008, Isotropic angle domain elastic reverse time migration: *Geophysics*, **73**, no. 6, S229–S239.
- Zhe, J., and S. A. Greenhalgh, 1997, Prestack multicomponent migration: *Geophysics*, **62**, 598–613.